Hindawi Publishing Corporation
EURASIP Journal on Advances in Signal Processing
Volume 2010, Article ID 317216, 14 pages
doi:10.1155/2010/317216

Research Article

A Study of Concrete Hydration and Dielectric Relaxation Mechanism Using Ground Penetrating Radar and Short-Time Fourier Transform

W. L. Lai, T. Kind, and H. Wiggenhauser

BAM, Federal Institute for Materials Research and Testing, Unter den Eichen 87, 12205 Berlin, Division VIII.2, Germany

Correspondence should be addressed to W. L. Lai, wai-lok.lai@bam.de

Received 7 January 2010; Revised 6 June 2010; Accepted 5 July 2010

Academic Editor: João Marcos A. Rebello

Ground penetrating radar (GPR) was used to characterize the frequency-dependent dielectric relaxation phenomena in ordinary Portland cement (OPC) hydration in concrete changing from fresh to hardened state. The study was experimented by measuring the changes of GPR A-scan waveforms over a period of 90 days, and processed the waveforms with short-time Fourier transform (STFT) in joint time-frequency analysis (JTFA) domain rather than a conventional time or frequency domain alone. The signals of the direct wave traveled at the concrete surface and the reflected wave from an embedded steel bar were transformed with STFT, in which the changes of peak frequency over ages were tracked. The peak frequencies were found to increase with ages and the patterns were found to match closely with primarily the well-known OPC hydration process and secondarily, the evaporation effect. The close match is contributed to the simultaneous effects converting free to bound water over time, on both conventional OPC hydration and dielectric relaxation mechanisms.

1. Introduction

1.1. Study of Materials Using GPR. Nondestructive testing methods attract many attentions in civil engineering applications rapidly in recent years [1, 2]. One of the most widely used methods is ground penetrating radar (GPR) which images and sees through material structures [3, 4]. Literatures have been reported extensively in the application on concrete structures such as bridges [4], railway ballast [5, 6], dams [3], and brick [7]. Principles of GPR were widely documented and reviewed [1, 2, 8, 9]. While most published works and field applications focused on locating internal characteristics (such as concrete reinforcement, voids and layer thickness), there is comparatively little effort to study the material properties which usually refers to the host materials, that is, concrete. From material's perspective, the mechanism converting water from free to bound form in OPC concrete was characterized with GPR by measuring the change in the real part of dielectric permittivity/velocity in time domain [10]. In this paper, we attempted to characterize the same mechanism by measuring the changes of frequency-dependent absorption and relaxation spectra which are affected by the imaginary part of material's permittivity.

Research on the material properties of concrete using the dielectric properties is normally in a localized scale and small volume of concrete, such as microwave terminal [11, 12] or dielectric sensor [13]. Larger-scale investigations should involve GPR which was used to assess the mechanism of hydration [10], concrete composition [14], moisture contents [15, 16], and pore size distribution [17].

1.2. GPR Signal Processing Method to Evaluate Material Properties. Most well-established GPR signal processing methods (such as time-zero correction, filtering, gain control, deconvolution, etc.) put emphasis on enhancing signal quality and understanding of the internal characteristics. In most cases, the ultimate goal of these methods is to reconstruct understandable signals in time domain which reveal the internal and spatial concrete structure. The first step is to stack one-dimensional GPR waveforms (A-scan) laterally to construct two-dimensional (B-scan) radargram, and followed by building three-dimensional cube views

(C-scan) after alignment of multiple B-scans [4]. B-scans and C-scans have been frequently used to delineate and interpret the internal characteristics of the spatial material structures, provided that the features exhibit contrasting electric properties compared to the host material. However, the B- and C-scans operated in time domain are unable to study the frequency features of the time-varying GPR signals, which are largely affected by the spatial or temporal changes of the concrete properties. In other words, when the interpretation of GPR signals is extended from object's location and spatial characterization to the study of material properties, the time domain method may not be adequate because the characteristic of the time-varying frequency is not taken into account. As such, this paper adopted a two-dimensional joint time-frequency analysis (JTFA) to transform and evaluate the signal. This method is based on and back to the most fundamental A-scan waveforms.

In the JTFA domain, we migrated the A-scans (obtained from 1.5 and 2.6 GHz GPR antennae) from one dimension (time) to two dimensions (time and frequency). In such domain, the localized frequency changes are analyzed jointly with the localized amplitude changes registered in the radar time axis (i.e., A-scan). Short-time fourier transform (STFT) was used as the computation algorithm because it allows the frequency spectra to be revealed in a preselected, stepped, and short-time windows compared to traditional Fourier transform. The sweeping of this short-time window over the radar time axis stacks the localized frequency spectra centered at each radar time points, and ultimately compiles a 2D time-frequency plot with time and frequency being the x- and y-axis. In this paper, the usefulness of this methodology is experimented with the well known cement hydration mechanism in concrete. It is well-known that concrete hydrates free water in concrete over the curing processes, and changes the wave propagation velocity, real part of permittivity and dielectric contrast [10]. In this paper, we measured the temporal changes of the A-scans over a period from an initial fresh state to a hardened state up to 90 days. Then the A-scans were processed and transformed to 2D time-frequency plots to observe the lateral frequency changes for both direct wave and an embedded steel bar reflector. These signals were further characterized and quantified by determination of the peak frequency, and justified by the dielectric relaxation and OPC hydration theories.

2. Theories

2.1. Ground Penetrating Radar (GPR). A GPR is an instrumentation tool that produces high-frequency electromagnetic waves propagating through the host materials. These waves are subjected to a combined effect of transmission, reflection, refraction, scattering, absorption, and attenuation by the materials which are usually dielectrics, such as concrete, soils, and rocks. The reflected energy is then captured, recorded, and digitized by a receiving antenna, and is registered as an amplitude record over the time windows in a scale of nanosecond, or simply known as an A-scan.

At frequency range in GHz level, the GPR wave propagation velocity and attenuation in a medium are primarily governed by the dielectric permittivity (ε) of the composite medium, as illustrated by the GPR plateau in [18]. The ε of any composite material is determined by the volumetric fraction of each individual ε, namely, air, water, and solids, and may be mathematically formulated by different dielectric mixing models [19]. In a dielectric, water is recognized as the single most dominant factor to change ε' [10, 14–17, 20]. Other factors are (1) electromagnetic (EM) frequency [21–24], (2) water to cement ratio [10, 14, 25], (3) porosity [17, 25], (4) ions in pore solution which make the material behave as lossy dielectrics [26], and (5) clay minerals of wide range of porosities and specific surfaces [27]. Because of the dominant effect of water on GPR wave propagation, GPR becomes a good candidate to solve the inverse problems of material properties, in particular about characterization of the changes of state of water in any porous cultural and natural materials with low conductivities, such as concrete, asphalt, and soil.

2.2. Cement Hydration. The change of free to bound state of water in concrete is best realized in the cement hydration process in concrete. For concrete after fresh mixing, curing starts to allow continued absorption of water by cement to develop and formulate dense solid calcium silicate hydrates (C-S-H). As the volume of C-S-H increases, the gel and capillary channels are blocked, segmented, and isolated. Free water is reduced, absorbed, and bounded because water is hydrated to change from free to bound form [28]. For OPC concrete, this mechanism is quick at initial stage and slows down afterwards. This process is vital for the development of concrete strength and durability which determines the structural integrity and the serviceability.

2.3. Frequency-Dependent Dielectric Relaxation in Porous Materials. When an electrical field is applied on a nonconductive material, the frequency dependence of the polarization process is described by permittivity relaxation phenomena and is characterized by the relaxation frequency (τ_f) of the material. Below τ_f, the particles are capable of being polarized instantaneously to the applied E-field and stay in phase with the E-field. Above τ_f, the frictional and the inertial effects cause this polarization to lag behind the E-field. It becomes no longer instantaneous [19] and therefore manifests a phase difference between the applied E-field and response polarization. Hence the dipole orientation as a bulk fails to fully contribute to the total polarization [29]. This phenomenon is known as dielectric dispersion of the dipolar/orientation polarization [30]. In the GPR frequency range (10 to 3000 MHz), most materials yield permittivity relaxation mechanism by remarking a decrease in the real component of complex permittivity, as formulated by Debye's model shown in Figure 1. At the same frequency, the imaginary component rises until reaching the peak frequency (τ_f) and drops afterwards. τ_f is governed by relaxation time τ_t; where $\tau_f = 1/2\pi\tau_t$ [29, 31]. At τ_f, the absorption mechanism of the material is most prominent.

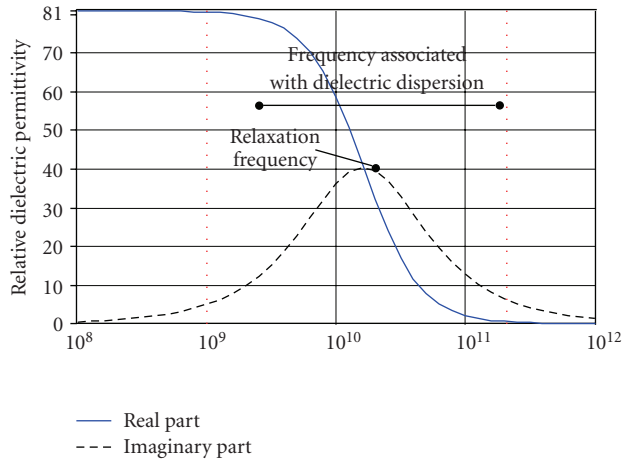

Figure 1: Graphical presentation of the Debye's model in liquid water.

The effect of the above mechanism was mathematically derived by Debye model [21], and Cole and Cole's (1941) models [32]. The former is used to model a pure material with single and well-defined polarization mechanism (Figure 1), while the latter models composite material manifesting different regions of dielectric dispersion and a spectrum of relaxation time. Ranges of τ_f for different materials were extensively studied, and that of free water is the highest compared to other composite materials containing water across the microwave region [33]. Its value is reported to be 17.1 GHz at 25°C [34]. Within the permittivity spectrum as a function of frequency, permittivity loss due to a composite material containing free water starts to be prominent at above 500 MHz [35].

The range of dielectric relaxation of composite materials with bound water (such as clayey soil) is much smaller than that with free water (such as sandy soil) [36–38]. It is because the bound water is limited in motion by electrostatic interaction with neighbouring solid particles, while the free water in the latter is not restricted [37]. It follows that the dielectric dispersion and relaxation frequency of a material are governed by the forms of water (i.e., bounded or free) in a material [35]. This well-known dielectric phenomenon is manifested in any porous material with water saturation, where loss mechanism and the associated relaxation frequency are shifted to a frequency much lower than that of free water (i.e., 17.1 GHz). It has been observed in soils, clays, and rocks [39–43], but is still not well understood in concrete. The effect depends on the degree of saturation, the form and distribution of the mineral phases (percentage of clay and rock particles). In concrete, it depends on the mix design and rate of change of turning majority of water from free to bound form.

2.4. Fourier Transform (FT) and Short-Time Fourier Transform (STFT). A signal processed with the classical Fourier transform is transformed to a plot showing the frequency distribution over the entire signal window. It is compared to sinusoidal functions, which spread over the entire signal in time domain and are not concentrated in any particular time. Therefore, the classical Fourier transform does not explicitly reveal how the frequency contents evolve with time when the signal is nonstationary [44]. To overcome this deficiency, JTFA is required to transform the one-dimensional signals into a two-dimensional time-frequency plot, in which STFT is one of the most widely used algorithms in JTFA based on detail Fourier transform centered at each time point. In STFT, the signal is compared with window functions that are concentrated in both time and frequency domains. The spectra at any particular time are then stacked to reflect the lateral variation of signal behavior in both time and frequency in JTFA. The STFT algorithm and the window function can be mathematically represented as (1) [45]

$$\mathrm{STFT}[x(t)] \equiv X(\tau,\omega) = \int_{-\infty}^{\infty} x(t)\omega(t-\tau)e^{-j\omega t}dt, \quad (1)$$

where $\omega(t)$ is the window function (e.g., a Hanning window) which has a user-defined short-time duration, and $x(t)$ is the signal in time domain. The length of this window is of vital importance and subject to the wavelength of the GPR frequencies. If the window length is too short, spectral leakage of low-frequency component appears; when it is too long, the target of interest would be blurred. $X(\tau,\omega)$ is the Fourier Transform of $x(t)w(t-\tau)$, a complex function representing the phase and magnitude of the signal over time and frequency. The right equality of (1) is an inner product which reflects the similarity between signal $x(t)$ and the elementary function $\omega(t-\tau)e^{-j\omega t}$. If the time duration and frequency bandwidth of $\omega(\tau)$ are Δ_t and Δ_ω, respectively, $\mathrm{STFT}[x(t)]$ in (1) indicates the signal's behaviors in the vicinity $[t-\Delta_t,\ t-\Delta_t]$ and $[\omega-\Delta_\omega,\ \omega-\Delta_\omega]$, where Δ_t is governed by the width of the window function.

3. Specimens and Instrumentation

Normal concrete with ordinary ASTM Type I OPC (CEM 32.5) was used in the experiment. The mix proportion includes 285 kg/m^3 cement, 170 kg/m^3 water (yielding a water to cement ratio 0.6), 1867 kg/m^{3}well-graded fine and coarse aggregate, and 0.91% lignosulfonates superplasticizer for enhancement of the workability. The average 7-day and 28-day strengths for measurements on three cubes for each were 31.3 MPa and 45.8 MPa, respectively. A concrete specimen with size 1.5 m long, 500 mm width, and 500 mm height is shown in Figures 2 and 3. Twelve other 150 mm cubes were casted to measure the 7-day, 28-day strengths, and regular measurements of weight in cover-cured and water-cured conditions (3 for each condition). The 1.5 m long specimen was enclosed and sealed with a thick plastic sheet to isolate the concrete from the environment throughout the measurement period, and to minimize the evaporation effect, within which a steel bar (25 mm diameter) was positioned at 100 mm below the concrete surface. There are some other bars inside the specimens installed for other purposes. But the remaining bars are at least 160 mm apart from the target bar and do not impose any effect on the measured GPR signal because of the small radiation

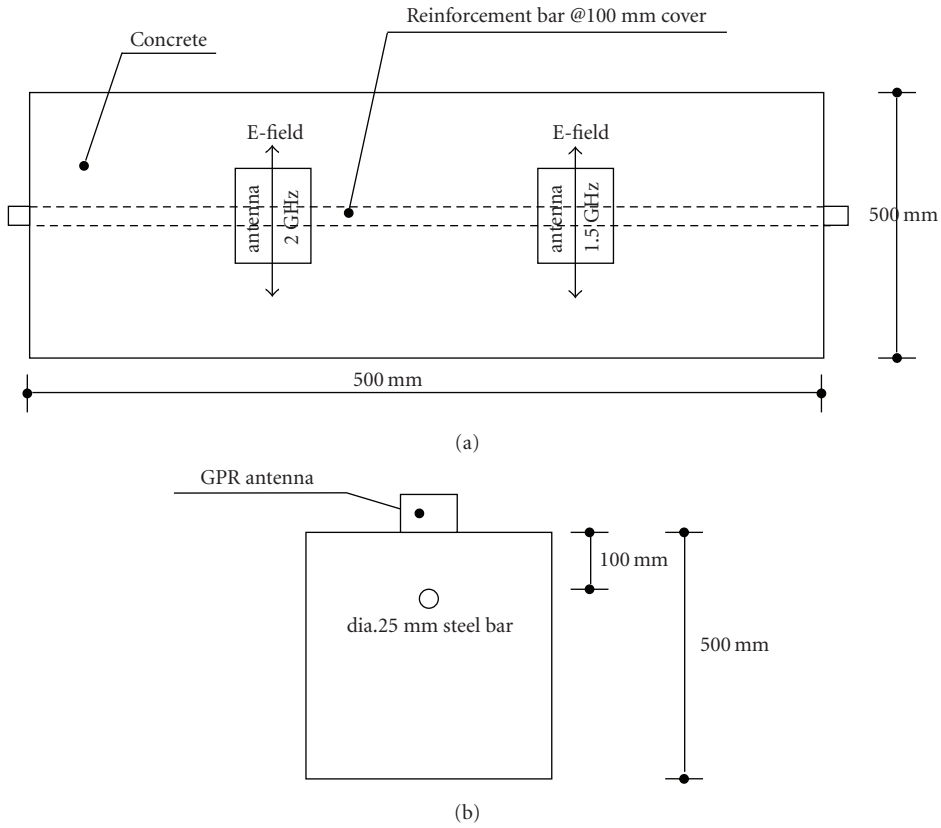

Figure 2: Plan view (a) and section (b) of the concrete specimen.

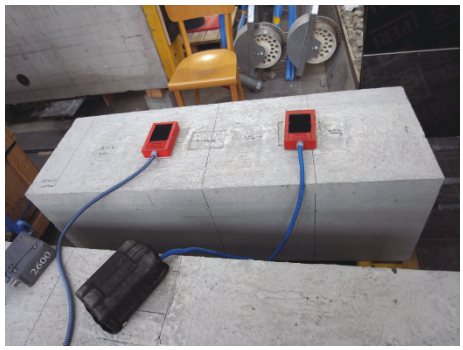

Figure 3: Overview of the specimen.

footprint illuminated by the high-frequency antenna. The concrete was cured in air over the test period. GPR antenna array was aligned perpendicularly on top of the concrete. At the initial fresh state (just after mixing), the antennae were over-hanged in position to avoid sinking into the surface concrete. The antenna arrays operated in nominal frequencies 1.5 and 2.6 GHz and connected with Geophysical Survey System Inc. (GSSI) SIR-20 dual channel GPR system. Selections of these GPR frequencies (the highest amongst the whole GPR frequency range) were justified because of its close proximity with the relaxation frequency (Figure 1) of free water, which makes the relaxation effect more readily observable.

4. Data Processing

4.1. Dewow Filtering, Direct Current Drift Correction and Time Zero Correction. All GPR A-scan signals (with time step = 39.1 ps and time window 10 ns) were firstly processed with an adjustment of direct current (DC) shift and dewow filter in time domain. These two procedures filtered the DC bias and low-frequency energy [9]. The second step is to assign a correct time zero position at the first reflected wave. The time zero was defined by firstly differentiating the A-scan twice to obtain the second derivative of the original A-scan, as shown in Figure 4. Then, over the first arrival direct wave (or direct wave because high-frequency GPR was used), the positions where sign changes from positive to negative in the 2nd derivative (i.e., the inflection point of the A-scan) were determined and were then feed back to the original A-scan. This point was defined as the real time zero because it demarcates the change from low frequency (being concave upwards) to high frequency (being concave downwards) when the direct wave enters from air to a dielectric medium, as illustrated in Figure 5. It is important to note that this low frequency component was not filtered by the DC shift and dewow filters. Also in the context of low frequency-antennae, the first wave is normally referred as a summation of wave traveling from the transmitter to receiver, and the wave over the surface concrete.

The above method is justified by an independent experiment using a concrete specimen (same mix as described

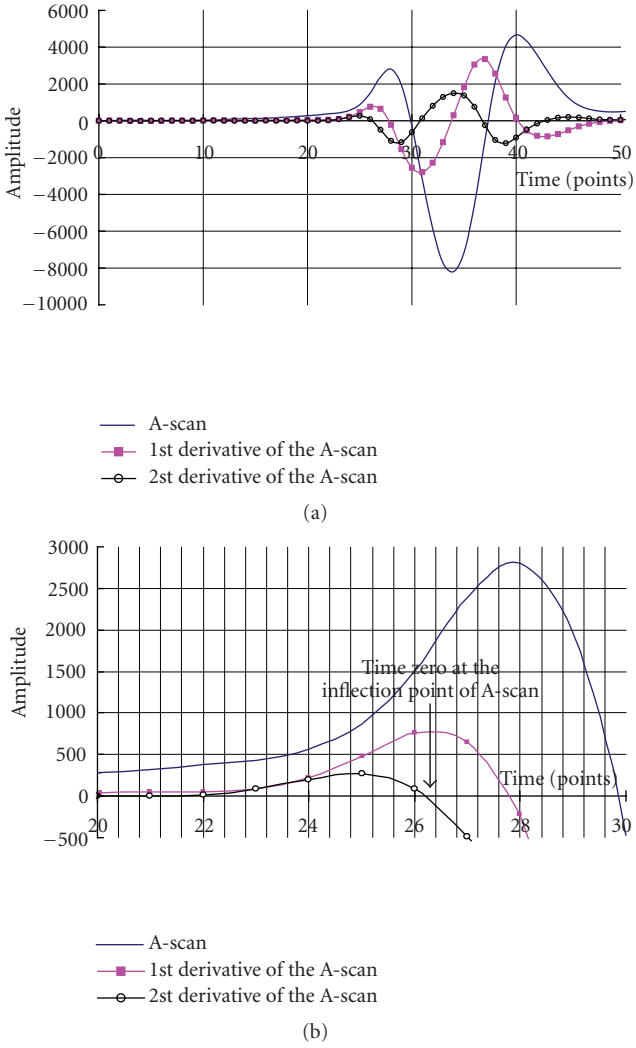

Figure 4: (a) 1.5 GHz A-scan and its first and second derivative. (b) 2.6 GHz A-scan and its first and second derivative (close-up view).

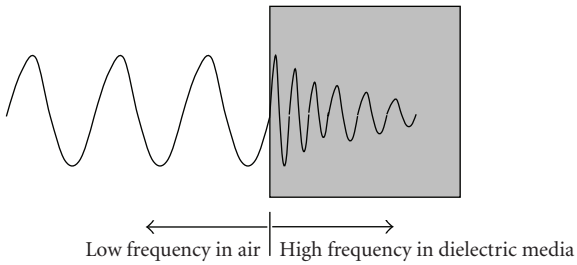

Figure 5: Change of low to high frequency of wave incident from air to dielectric media.

in this paper) with two steel bars at two cover depths (25 mm, 50 mm). A-scans collected on top of the two bars were directly subtracted by those without bars. The result is shown in Figure 6. The position of zero-crossing at the bar reflection was defined as the position of the reflector [45]. It was determined, and then back-calculated linearly to the true time zero corresponding to the surface position.

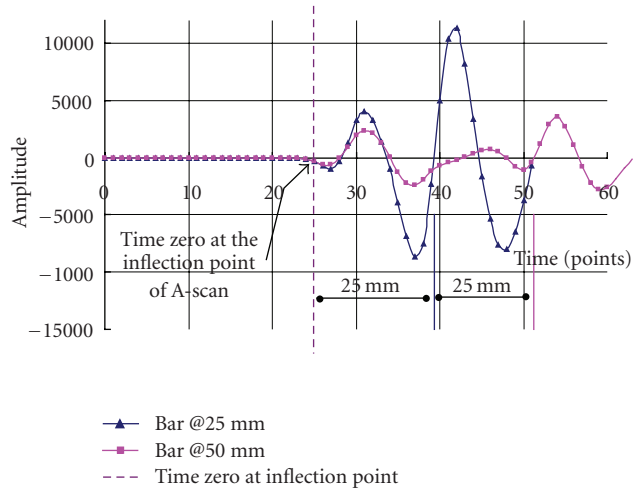

Figure 6: Subtracted 2.6 GHz waveforms (with and without bars) for bars at 25 mm and 50 mm.

Comparison between the calculated time zero position and the inflection point method yields a difference less than 20 ps. This accuracy should be able to justify the credibility of the inflection point method to correct the time zero. Also noted in Figure 6, the minor reflections before the zero crossing of the bars are due to the slight phase shift between the A-scans captured with and without bars.

4.2. Fourier Transform (FT) and Short-Time Fourier Transform (STFT). Fourier transform was applied to every A-scan to observe the distributions of frequency components (arisen from clutter/signal ringing, direct wave, and steel bars) over the original A-scan function, after zero-padding to 4096 points, and no windowing function nor filtering was applied at this stage. But for signal transformation with STFT, a temporal finite impulse response (FIR) high-pass filter was applied to filter the prevalent clutter/ringing which locates in the low-frequency regime. Also, every one-dimensional GPR A-scan was windowed with a short Hanning window which is low aliasing. We adopt the size of the Hanning window being *eight* times of the time taken from first peak to first valley (or 1/2 wavelength) in the direct wave. This is an objective measure independent of manual selection of time window, which alleviates and reconciles the trade-offs regarding the spectral leakage (due to too small time window), and unclear target of interest (due to too large time window) in STFT spectrogram and influence by other neighbouring frequency component. Within a reasonable range of time window, a larger window size in our program yields a smaller peak frequency, though the difference is minimal. For example, with an input signal centered at 2 GHz, a window size spanning from 1ns to 3 ns in STFT yields a center frequency ranging from 2070 to 1970 MHz, respectively. The windowed mathematical function was then transformed according to (1) and Figure 7. The frequency spectrum was then stacked to plot a 2D STFT spectrogram in JTFA domain (Figure 8(a)). At every frequency step, a Gaussian gain function centered at the peak

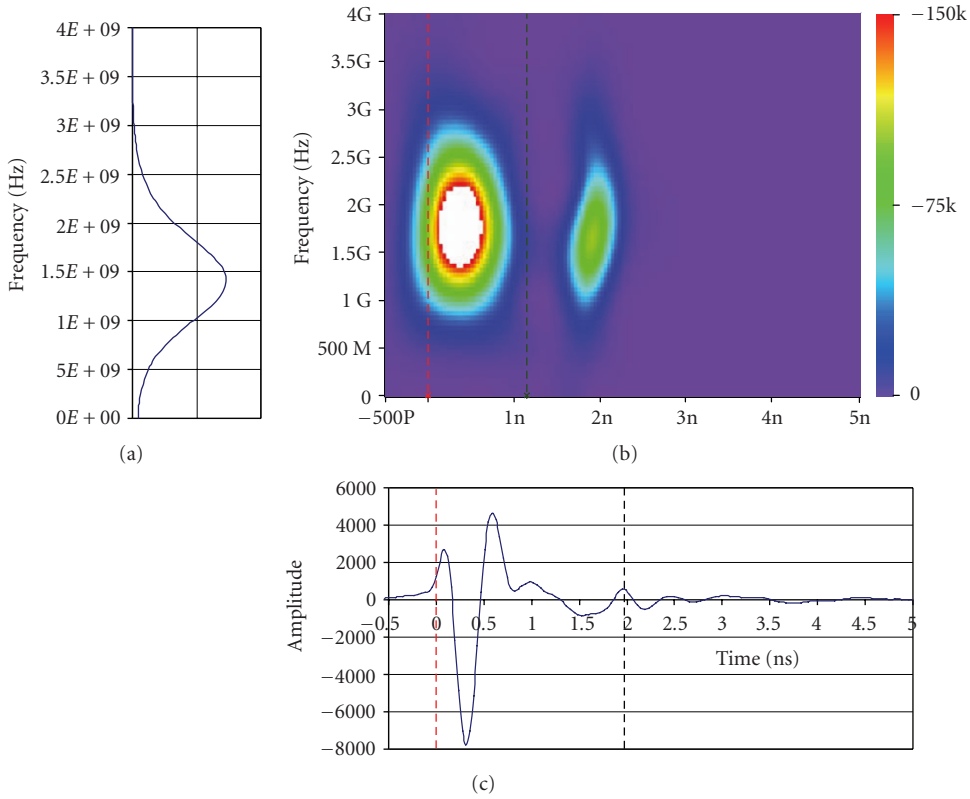

Figure 7: Frequency spectrum at 2.1 ns (a), 2.6 GHz STFT spectrogram (b), and GPR A-scan (c), at day 7.

location of the bar reflection (Figure 8(c)) was multiplied on the spectrogram (Figure 8(a)) to stand out the bar signals which were originally much weaker than the high intensity of the direct wave (Figure 8(b)). Gaussian functions were determined specifically for each dataset, in which the maximum amplitudes of the functions were based on dividing the maximum amplitudes of the direct wave by the bar reflections in JTFA domain.

5. Findings

5.1. Time Domain A-Scans. Figure 9 shows the A-scans collected at different days after fresh mixing. The collection of data was started once every day from fresh state to day 7, and then once at days 14, 28, 56, and 90 Positions of the bar reflections were identified by comparing the reflections when the antenna was captured on top of the bar and on top of other locations with plain concrete only. The bar reflections were ill defined in time domain from the fresh state to day 4 because high water content caused more attenuation suffered by the high-frequency GPR antennae. This is improved after day 5, where the reflections started to be well defined, and therefore only data from days 5 to 7, 14, 28, 56, and 90 are presented in Figures 9 and 10. Along with age, the reflections from the bar traveled much faster (shorter time) and exhibited a larger intensity. It is because the majority of free water was progressively consumed and bound to formulate the structure of calcium silicate hydrate, while a small part of the water evaporated. Details of the consumption of these two parts of water will be discussed in Section 5.4. This mechanism was described by a mechanistic model which takes both dielectric and hydration perspectives into account [10].

5.2. Fourier Transform (FT) Over the Entire Time Window. Time domain A-scans were transformed to frequency spectra through FT, as illustrated in Figures 11 and 12. The frequency amplitude was normalized by the maximum amplitude of day 90's data, so that the tendency of the growth of the frequency component becomes immediately prominent. For both 2.6 GHz and 1.5 GHz data, the one and wide-band frequency appeared at the fresh initial state dispersed into three distinct frequency localities along with ages. The lowest locality (below 1100 MHz at 2.6 GHz and below 800 MHz at 1.5 GHz FT) is arisen by the clutter and signal ringing. This clutter and ringing declined in amplitude in 2.6 GHz data, but increased in 1.5 GHz data along with ages. This reverse trend may possibly be due to different antenna design which is not of significant importance.

The middle and high-frequency localities were from the direct wave or bar reflection, which was however not possible to be distinguished according to FT plots alone. With the aid of STFT spectrogram in Figures 13 and 14, the nonstationary nature of the signals was revealed along the time and frequency axis. In the STFT spectrogram, the middle frequency locality refers to the range from 1.2 G to

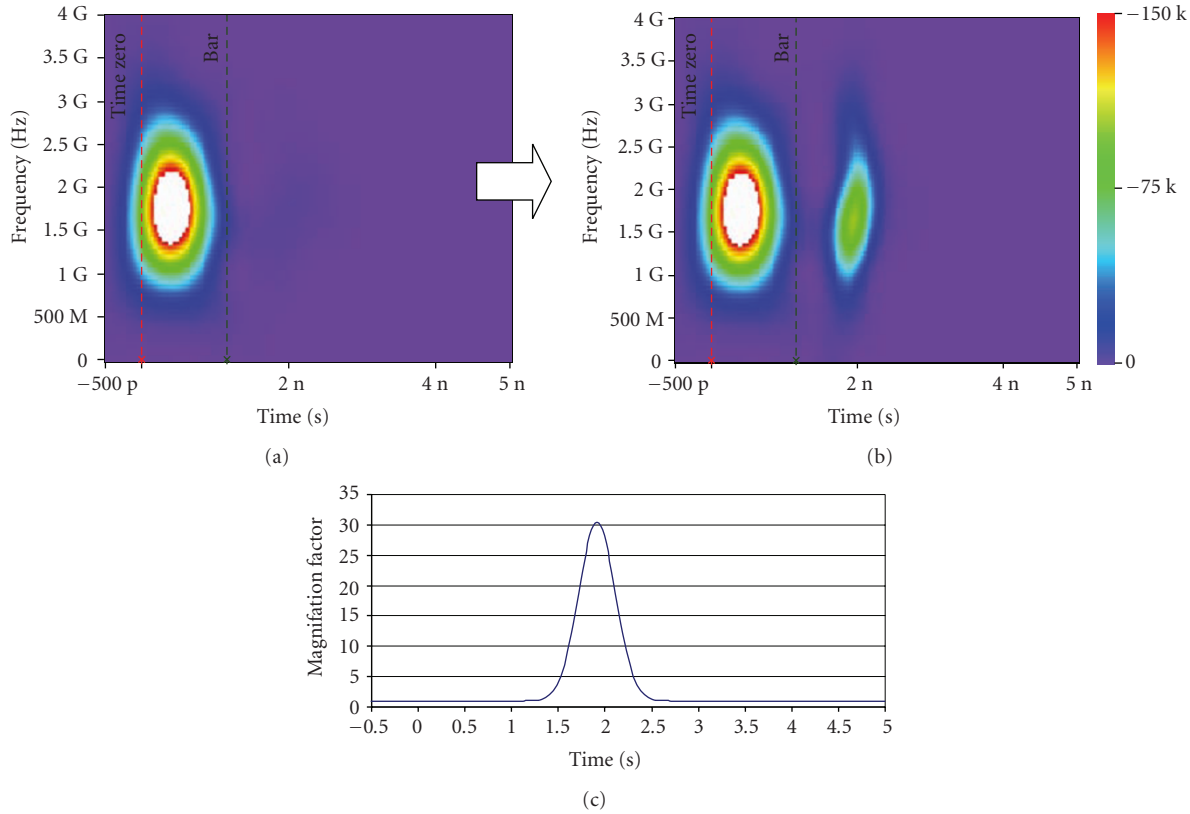

FIGURE 8: Original STFT spectrogram (a) and the enhanced STFT spectrogram (b) after applying Gaussian gain in JTFA domain at every frequency bin (c).

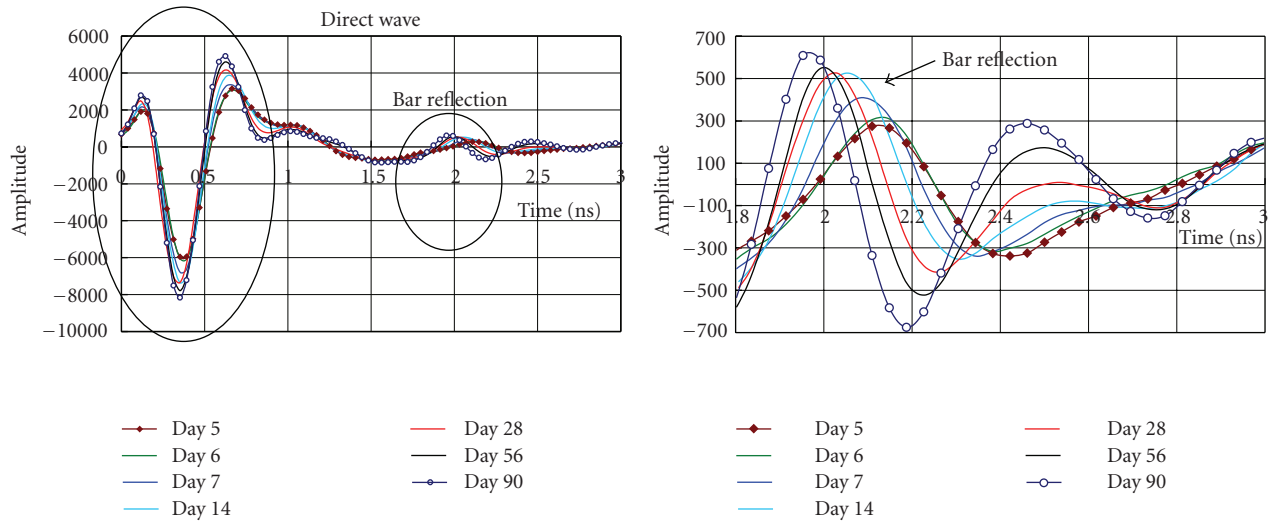

FIGURE 9: 2.6 GHz A-scan in time domain (reflections captured when the antenna was on top of the bar).

1.8 GHz for 2.6 GHz FT (shaded region in Figure 11), and from 800 MHz to 1.2 GHz for 1.5 GHz FT (shaded region in Figure 12). The localities beyond the upper threshold of middle locality are termed as the highest frequency locality. The FT middle frequency locality is corresponding to the bar reflection in 2.6 GHz FT (Figure 11). It increased in intensity and shifted to higher frequency with ages, but the same locality in 1.5 GHz FT was correspondent to the direct wave (Figure 12). On the contrary, the highest locality is attributed to direct wave in 2.6 GHz FT. Similar to the middle locality,

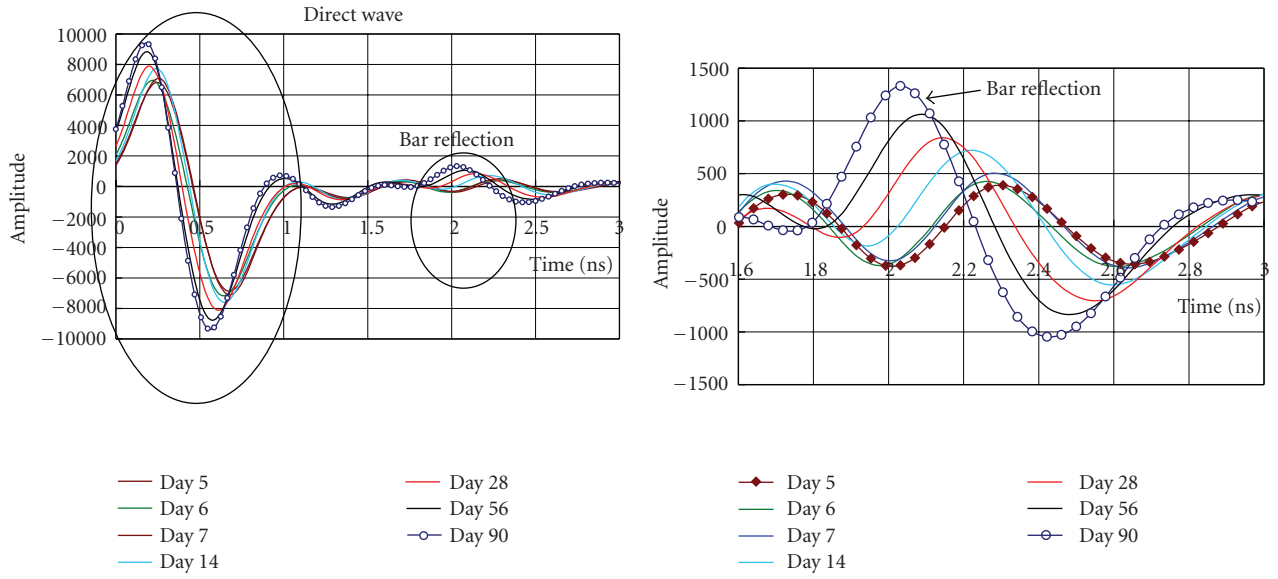

Figure 10: 1.5 GHz A-scans in time domain (reflections captured when the antenna was on top of the bar).

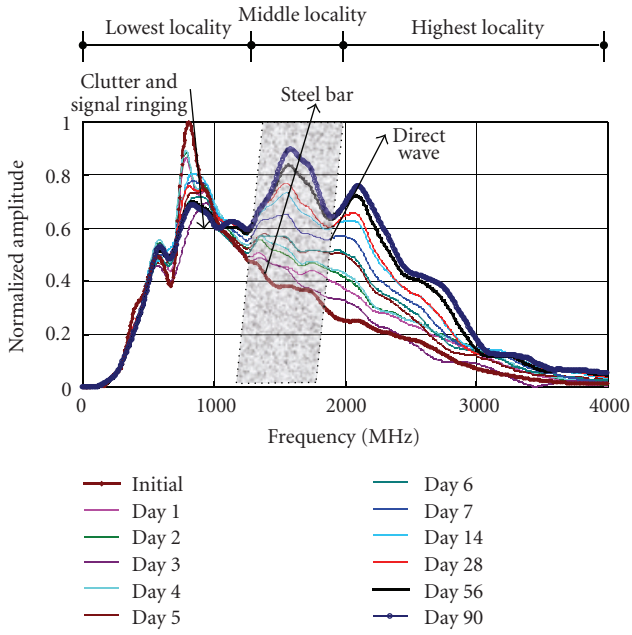

Figure 11: Frequency spectra of the entire A-scan captured by 2.6 GHz antenna.

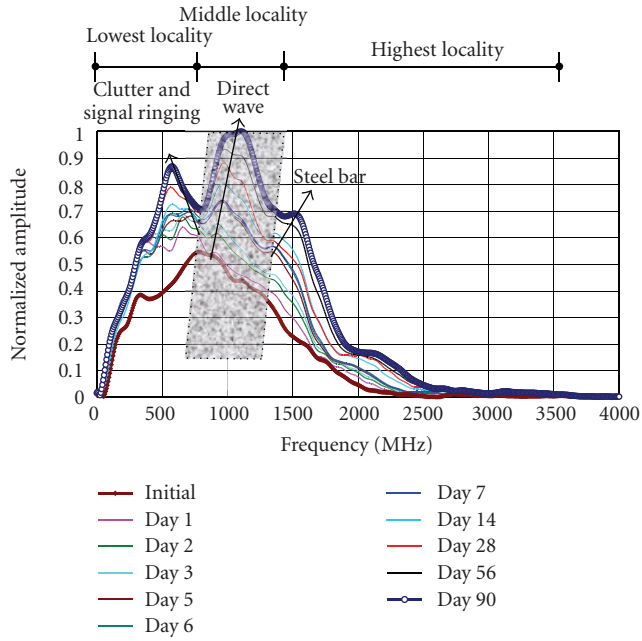

Figure 12: Frequency spectra of the entire A-scan captured by 1.5 GHz antenna.

it also increased in intensity and shifted to higher frequency with age, but the same locality in 1.5 GHz FT was from the bar reflection.

5.3. Short-Time Fourier Transform Over Short-Time Window. In Figures 13 and 14, the FT low-frequency localities (due to clutter and ringing) were filtered out by applying a high-pass FIR filter for 2.6 GHz and 1.5 GHz data. The high-pass filter frequencies for each age were determined at which the frequencies reached the maximum over the lowest locality (clutter/signal ringing) in FT according to Figures 11 and 12.

The tendency of frequency shift shown in Figures 13 and 14 was further studied closely by plotting the STFT frequency spectra which centered the peak locations of direct wave and bar reflections, as reported in Figures 15 and 16. Depending on the ages, the peaks of the direct wave are centered at around 0.2 to 0.25 ns (time domain), and the peaks of the bar reflections are centered at approximately 2-2.3 ns (time domain). The values of both ranges are depending on the

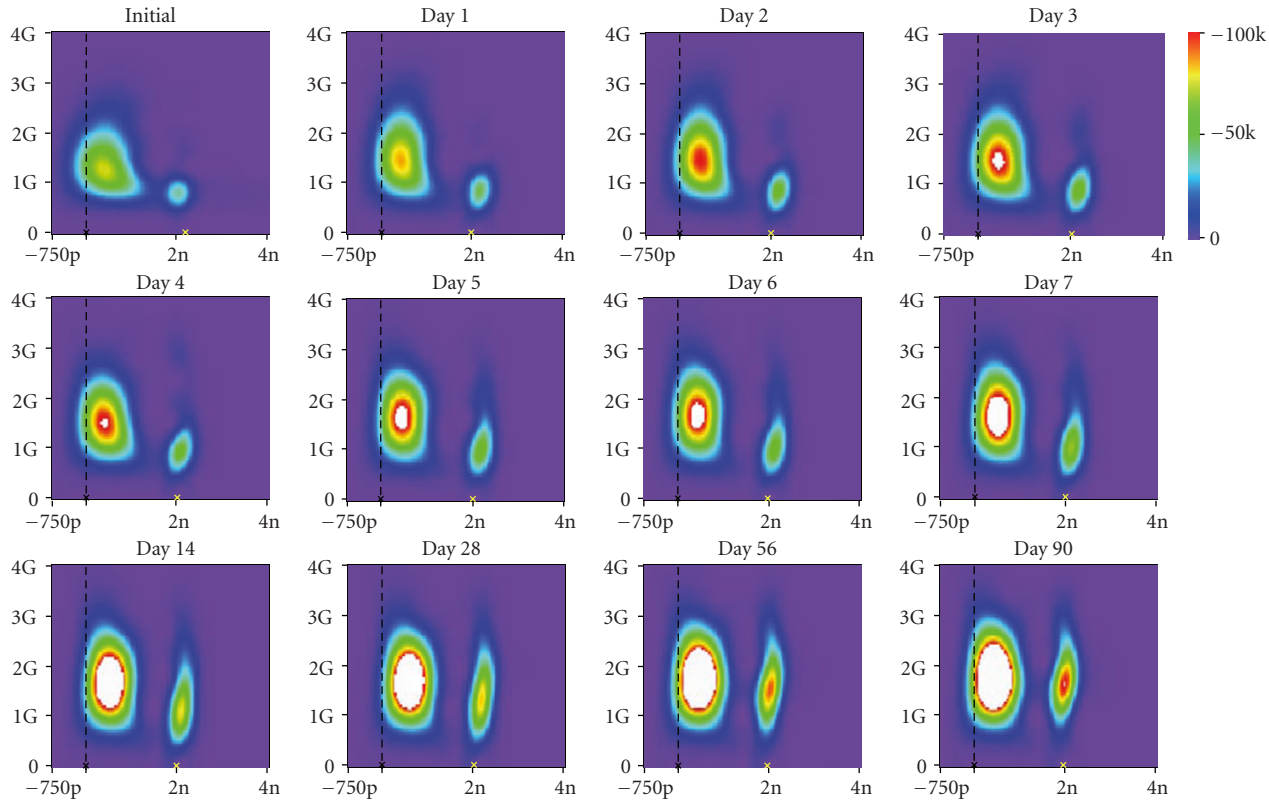

Figure 13: 2.6 GHz STFT spectrogram. x-axis is time (s), y-axis is frequency (Hz), and z-axis is the signal intensity with the same scale for all STFT spectrograms. The broken vertical line is the location of time zero. Gaussian gains were applied at the peak position of the bar reflections, which is approximately at 2.0 ns.

ages of concrete, as illustrated in Figures 9 and 10. The peak frequencies were then extracted to track the increase of peak frequency changes of the reflection over the ages, and plotted in Figure 17.

There are two important points to note. Firstly, the spectra measured in Figures 15 and 16 are indicative to and proportional with, but are not equal to, the actual spectra of imaginary part of permittivity. This is because the spectra were not directly determined by permittivity measurement tools, but with signal processing methods such as STFT algorithm. Different STFT methods (types and length of windows) can change the absolute values of the spectra. Secondly, it is clear for the FT plots, in which the increase of frequency intensity at the middle and the highest localities is due to the increase of amplitude in time domain, as discussed in Section 5.1. But most importantly, the direct wave and the bar reflections shifted to a higher-frequency regime which can be justified by the dielectric relaxation theory described in this paper.

5.4. Increase of STFT Peak Frequency with Ages. Concrete can be regarded as a low-pass filter for the input GPR signals, because frequency from a reflector's signal over a distance from the surface is always smaller than the direct wave at the surface [46], as depicted in Figures 13 and 14. On the other hand, when we compare the peak frequencies from the bar reflectors in different ages, the initial small peak frequency was found to shift to its higher-frequency regime. This increase over ages is attributed to the absorption of different frequency components in different concrete ages, and the associated change of relaxation frequency. In fresh and early age of concrete, water was in free form and its imaginary part tended to absorb high-frequency component of the GPR wave (which is close to water relaxation frequency [21, 33]), as shown in Figure 1. Therefore, the frequency spectra shown in Figures 15 and 16 started with values towards the low end. As concrete was hardened with time, free water became bounded and restricted to be polarized under the effect of high-frequency E-field. As a result, the high-frequency component was less attenuated and shifted the spectra to the higher end, yielding a higher value of peak frequency and wider bandwidth. The mechanism is illustrated in Figure 18. The rate of change of this process was proportional to the well-known cement hydration process which is a result of the process turning water from free to bound form. In fact, three of the four plots (2.6 GHz direct wave and bar reflection; 1.5 GHz bar reflection) in Figure 17 show sharp increases before day 7 and a gradual increase afterwards. The only exception is 1.5 GHz direct wave because it covers a longer radar time window and longer wavelength compared to the 2.6 GHz counterpart, as shown in Figures 9 and 10. Therefore, the long wavelength made

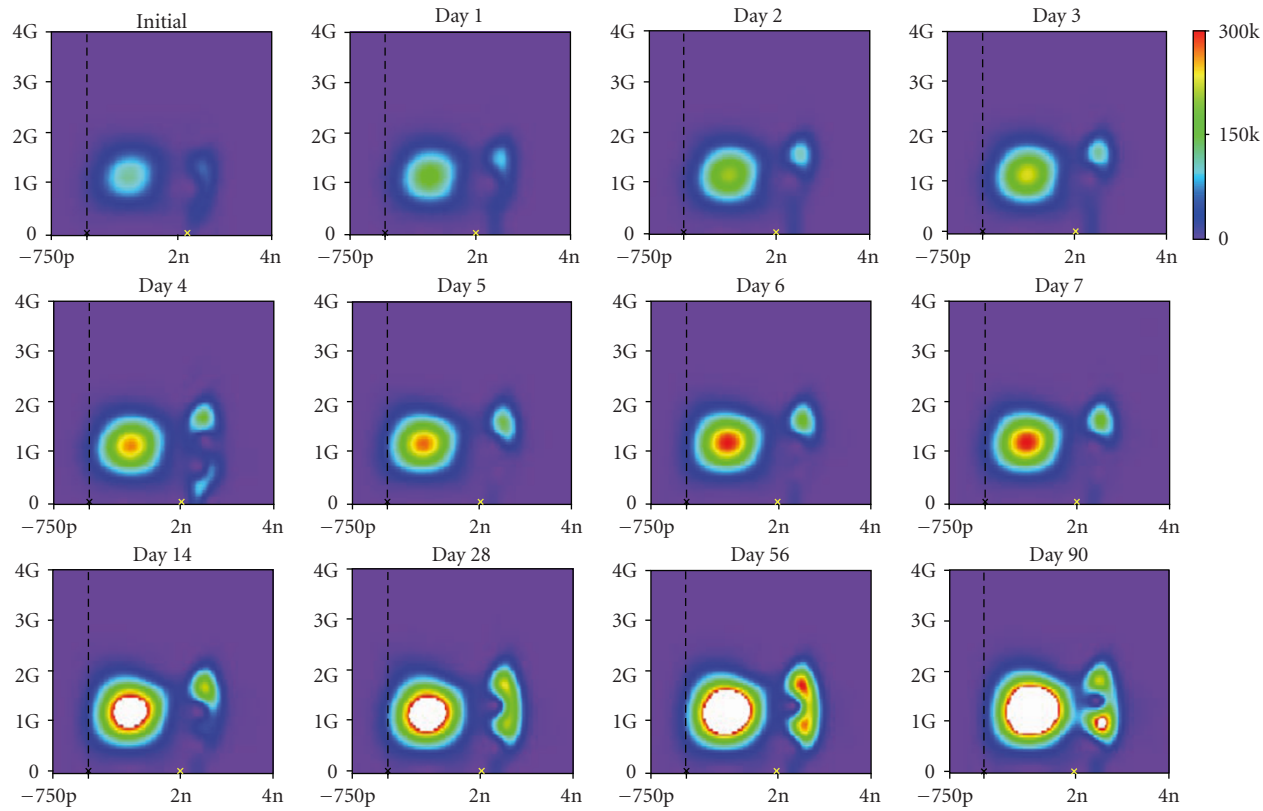

Figure 14: 1.5 GHz STFT spectrogram. x-axis is time (s), y-axis is frequency (Hz), and z-axis is the signal intensity with the same scale for all STFT spectrograms. The broken vertical line is the location of time zero. Gaussian gains were applied at the peak position of the bar reflections, which is approximately at 2.5 ns.

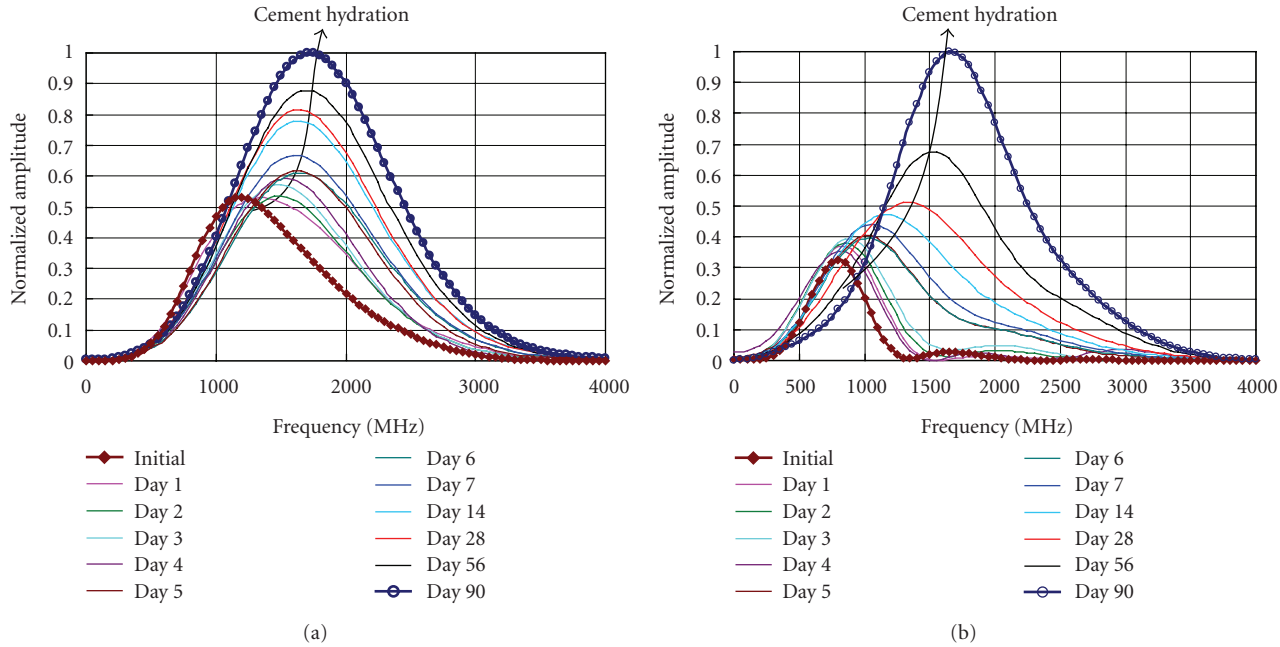

Figure 15: (a) 2.6 GHz STFT frequency spectra centered at the peak of direct wave. (b) 2.6 GHz STFT frequency spectra centered at the peak of steel bar.

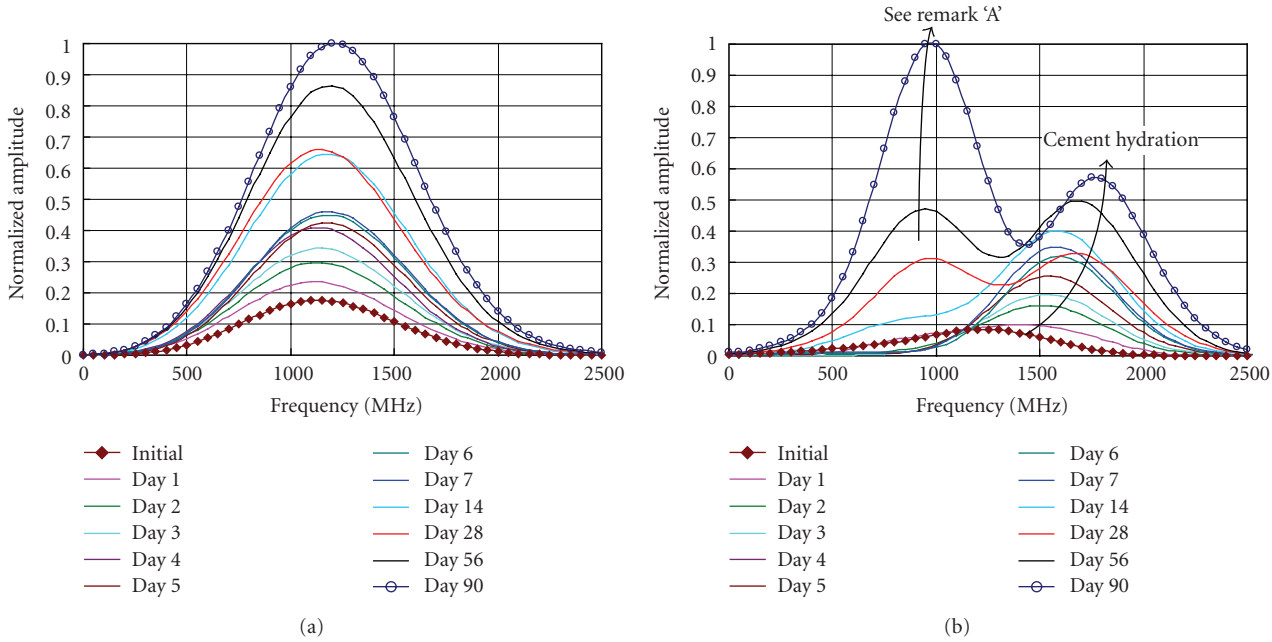

Figure 16: (a) 1.5 GHz STFT frequency spectra centered at the peak of direct wave. (b) 1.5 GHz STFT frequency spectra centered at the peak of steel bar reflection. In time (Figure 10) and JTFA domains (Figure 14), low frequency component rises since bar reflection approached to the trails of low-frequency direct wave which is stronger in later than early days.

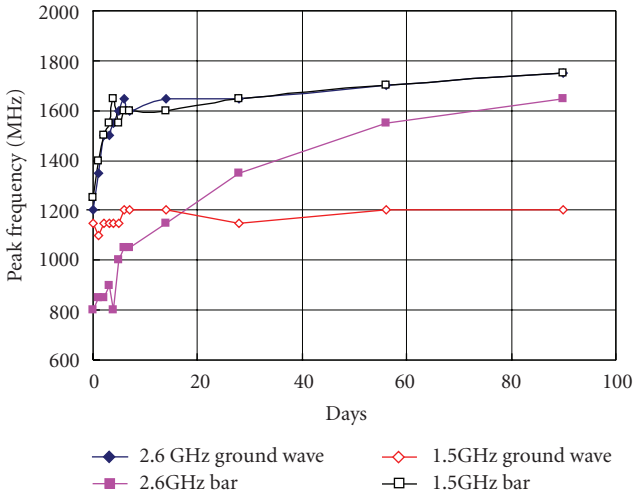

Figure 17: Change of peak frequency with the early age curing of concrete.

it not sensitive to changes of state of water, and exhibited unremarkable frequency changes over the lapsed time. Also in Figure 16(b), low-frequency component rose with ages because the bar reflections in time domain (Figure 10) and JTFA domain (Figure 14) approached to the low-frequency trails of direct wave which is stronger in later than early ages.

These curve shapes (except 1.5 GHz direct wave) in Figure 17 are very close to the well-known concrete hydration curves for OPC concrete. The OPC hydration curves mean a rapid increase in the first 7 days and a gradual increase afterwards. This is also evidenced experimentally by the rapid development of compressive strength (as a direct indicator of hydration) in the first 7 days (31.3 MPa at day 7) and gradual development afterwards (45.8 MPa at day 28). It is therefore concluded that the change of STFT peak frequency in the high GPR frequency regime can be used to characterize the cement hydration process nondestructively. A special remark about evaporation must also be noted. The water turned from free to bound water may be formulated by the approximation, assuming that change of weight is due to the form of water: *free to bound (hydrated) water = initial water content − evaporated free water − unhydrated free water contained*, where the following points exist.

(1) *Initial water content.* The design water content for fresh mixing is 170 kg/m^3. Given a fixed 150 mm cube in volume, this amount equals to 573.8 g (=170 kg/m^3 × 0.15 m × 0.15 m × 0.15 m).

(2) *Evaporated free water.* For 150 mm cube's weight measurement throughout 90 days, and based on the difference between cover- and water-cured concrete, 83.8 g (14.6% of initial water content) was lost due to evaporation at day 90 (Figure 19 and Table 1). This loss would be much more if concrete is totally exposed to air, and therefore covering concrete with plastic sheet minimizes the effect of evaporation.

(3) *Unhydrated free water.* Standard 105°C oven-drying of the 90-day specimen shows that 62.9 g (11% of initial water content) of the water was still unhydrated, free, or absorbed in capillary, but not yet bounded.

Following this approximation, free to bound (hydrated) water equals 573.8 g (100%) − 83.8 g (14.6%) − 62.9 g

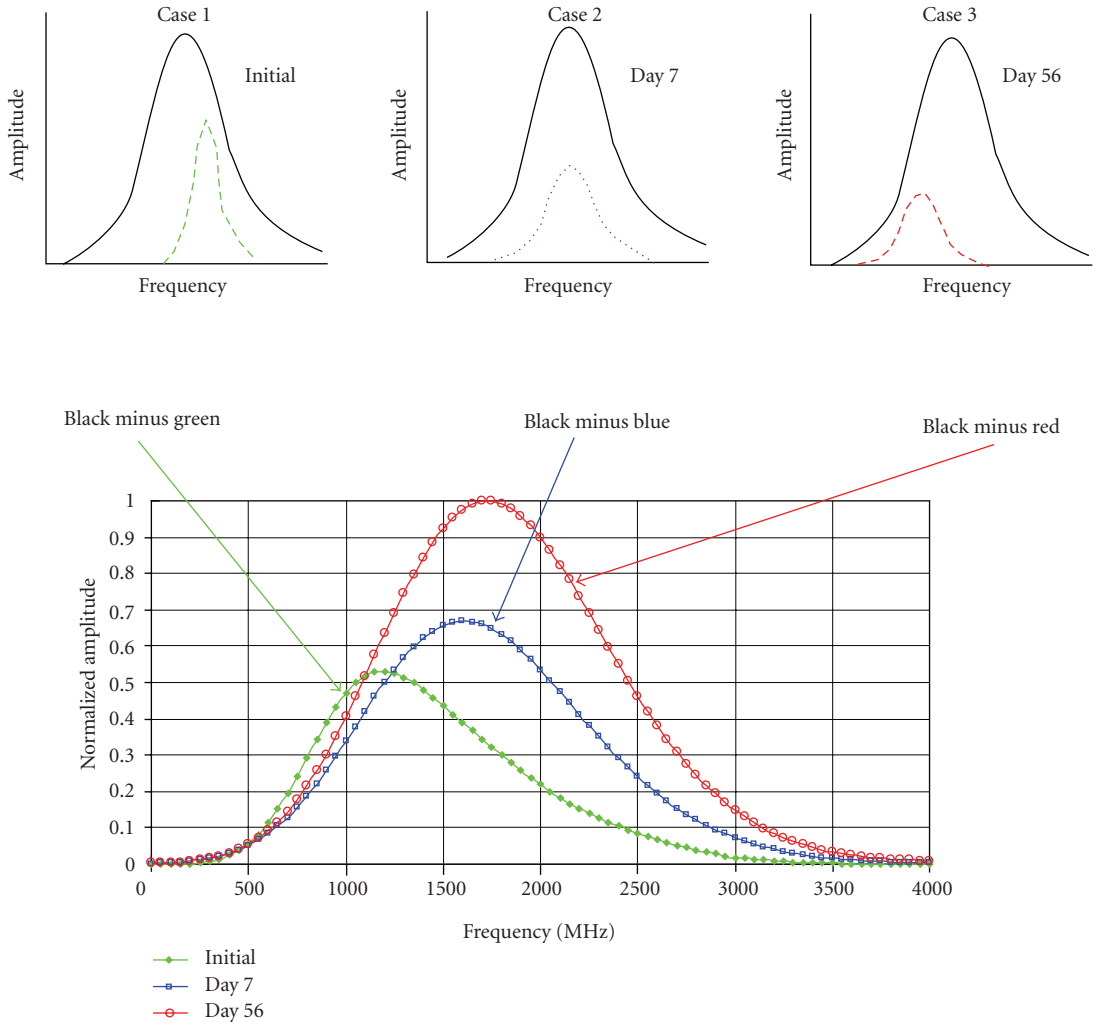

Figure 18: Spectrum change due to change from free to bound water in early-aged concrete. Case 1: All water is in free form. Case 2: Water is hydrated and bounded; free water still remains and absorbed in capillary. Case 3: More water is hydrated and bounded, but smaller amount of free water still exists in the capillary.

Table 1: Changes of concrete weight due to different curing conditions.

	Water-cured in curing tank		Cover-cured in room temperature and humidity		
Day	Weight (g)	Difference compared to initial (g)	Day	Weight (g)	Difference compared to initial (g)
Initial fresh state	7954,4	0,0	Initial fresh state	7954,4	0,0
2	7850,5	−6,5	2	N/A	N/A
3	7853,9	−3,1	3	7909,3	52,3
4	7856,7	−0,3	4	7880,3	23,3
5	7858,3	1,3	5	7867,0	10,0
6	7860,1	3,1	6	7860,4	3,4
7	7861,0	4,0	7	7854,0	−3,0
14	7861,8	4,8	14	7830,0	−27,0
28	7862,5	5,5	28	7810,5	−46,5
56	7863,1	6,1	56	7786,8	−70,2
90	7863,8	6,8	90	7780,0	−77,0

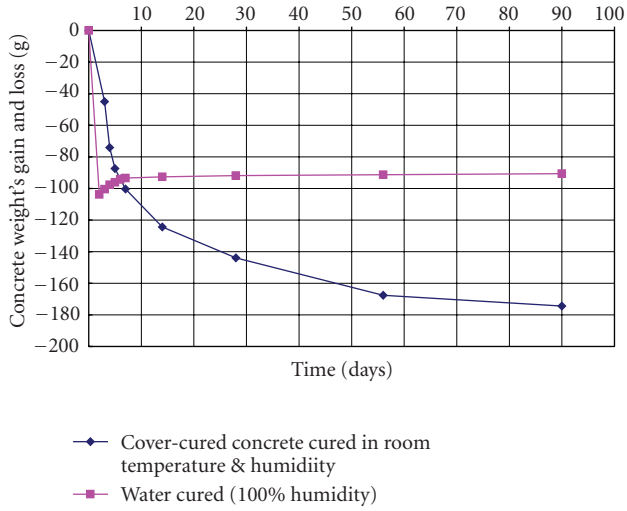

Figure 19: Changes of concrete weight due to different curing conditions.

(11%) = 427.1 (74.4%) as shown above, assuming that the weight change is solely dependent on the change of state of water (bounded or evaporated). This majority, along with the evaporated free water (14.6% minority) contributed to absorption of less high-frequency content (manifesting a shift to high frequency regime) in the frequency spectra. Transformation of free to bound form of water is surely minor in long term, but is definitely significant in early age (esp. from initial to day 7). One to one relationship is still yet to be developed, but nevertheless the trend is obvious.

6. Conclusions

The STFT method reported in this paper was used to analyze the time-varying GPR signals. This was achieved by measuring the changes of frequency spectra centered at in each time step over the radar time window, rather than applying classical fourier transform depicting the frequency spectra over the whole time window. With appropriate signal processing method, GPR can be used to study the hydration properties in OPC concrete. It is because the free or bound form of water yields a different but simultaneous effect on both dielectric relaxation and cement hydration mechanisms. The method can be further extended to study different hydration mechanisms of different concretes nondestructively, and on a much larger volume of materials compared to the small transmission line method. Most importantly, the method is not limited to OPC hydration, but may also be applied in various types of cement, water to cement ratios, and materials replacing part of OPC (such as fly ash and silica fume) that exhibit pozzolanic reactions.

References

[1] J. H. Bungey, "Sub-surface radar testing of concrete: a review," *Construction and Building Materials*, vol. 18, no. 1, pp. 1–8, 2004.

[2] V. M. Malhotra and N. J. Carino, Eds., *Handbook on Nondestructive Testing of Concrete*, CRC Press, Boca Raton, Fla, USA, 2nd edition, 2006.

[3] H. C. Rhim, "Condition monitoring of deteriorating concrete dams using radar," *Cement and Concrete Research*, vol. 31, no. 3, pp. 363–373, 2001.

[4] C. Kohl and D. Streicher, "Results of reconstructed and fused NDT-data measured in the laboratory and on-site at bridges," *Cement and Concrete Composites*, vol. 28, no. 4, pp. 402–413, 2006.

[5] T. Kind, "Study of the behaviour of a multi-offset antenna array on railway ballast," in *Proceedings of the 12th International Conference on Ground Penetrating Radar (GPR '08)*, Birmingham, UK, 2008.

[6] I. Al-Qadi, W. Xie, and R. Roberts, "Optimization of antenna configuration in multiple-frequency ground penetrating radar system for railroad substructure assessment," *NDT and E International*, vol. 43, no. 1, pp. 20–28, 2010.

[7] Ch. Maierhofer and J. Wöstmann, "Investigation of dielectric properties of brick materials as a function of moisture and salt content using a microwave impulse technique at very high frequencies," *NDT and E International*, vol. 31, no. 4, pp. 259–263, 1998.

[8] D. M. McCann and M. C. Forde, "Review of NDT methods in the assessment of concrete and masonry structures," *NDT and E International*, vol. 34, no. 2, pp. 71–84, 2001.

[9] A. P. Annan, "Electromagnetic principles of ground penetrating radar," in *Ground Penetrating Radar: Theory and Applications*, H. M. Jol, Ed., chapter 1, Elsevier, Amsterdam, The Netherlands, 2009.

[10] W. L. Lai, S. C. Kou, W. F. Tsang, and C. S. Poon, "Characterization of concrete properties from dielectric properties using ground penetrating radar," *Cement and Concrete Research*, vol. 39, no. 8, pp. 687–695, 2009.

[11] K. Gorur, M. K. Smit, and F. H. Wittmann, "Microwave study of hydrating cement paste at early age," *Cement and Concrete Research*, vol. 12, no. 4, pp. 447–454, 1982.

[12] M. A. Rzepecka, M. A. L. Hamid, and A. H. Soliman, "Monitoring of concrete curing process by microwave terminal measurements," *IEEE Transactions on Industrial Electronics*, vol. 19, no. 4, pp. 120–125, 1972.

[13] V. A. Beek, *Dielectric properties of young concrete*, Ph.D. thesis, Delft University, 2000.

[14] M. N. Soutsos, J. H. Bungey, S. G. Millard, M. R. Shaw, and A. Patterson, "Dielectric properties of concrete and their influence on radar testing," *NDT and E International*, vol. 34, no. 6, pp. 419–425, 2001.

[15] G. Klysz and J.-P. Balayssac, "Determination of volumetric water content of concrete using ground-penetrating radar," *Cement and Concrete Research*, vol. 37, no. 8, pp. 1164–1171, 2007.

[16] S. Laurens, J. P. Balayssac, J. Rhazi, G. Klysz, and G. Arliguie, "Non-destructive evaluation of concrete moisture by GPR: experimental study and direct modeling," *Materials and Structures/Materiaux et Constructions*, vol. 38, no. 283, pp. 827–832, 2005.

[17] W. L. Lai and W. F. Tsang, "Characterization of pore systems of air/water-cured concrete using ground penetrating radar (GPR) through continuous water injection," *Construction and Building Materials*, vol. 22, no. 3, pp. 250–256, 2008.

[18] J. L. Davis and A. P. Annan, "Ground-penetrating radar for high-resolution mapping of soil and rock stratigraphy," *Geophysical Prospecting*, vol. 37, no. 5, pp. 531–551, 1989.

[19] M. D. Knoll, *A petrophysical basis for ground-penetrating radar and very early time electromagnetics*, Ph.D. thesis, The University of British Columbia, 1996.

[20] G. C. Topp, J. L. Davis, and A. P. Annan, "Electromagnetic determination of soil water content: measurements in coaxial transmission lines," *Water Resources Research*, vol. 16, no. 3, pp. 574–582, 1980.

[21] P. Debye, *Polar Molecules*, Chemical Publication Company, 1929.

[22] P. Hoeskstra and A. Delaney, "Dielectric properties of soils at UHF and microwave frequencies," *Journal of Geophysical Research*, vol. 79, no. 11, pp. 1699–1708, 1974.

[23] Concrete Society, "Guidance on radar testing of concrete structures," Tech. Rep. 48, Concrete Society, 1997.

[24] W. L. Lai, W. F. Tsang, H. Fang, and D. Xiao, "Experimental determination of bulk dielectric properties and porosity of porous asphalt and soils using GPR and a cyclic moisture variation technique," *Geophysics*, vol. 71, no. 4, pp. K93–K102, 2006.

[25] P. Gu and J. J. Beaudoin, "Dielectric behaviour of hardened cementitious materials," *Advances in Cement Research*, vol. 9, no. 33, pp. 1–8, 1997.

[26] D. J. Daniels, Ed., *Ground Penetrating Radar*, The Institution of Electrical Engineers, London, UK, 2nd edition, 2004.

[27] N. R. Peplinski, F. T. Ulaby, and M. C. Dobson, "Dielectric properties of soils in the 0.3-1.3-GHz range," *IEEE Transactions on Geoscience and Remote Sensing*, vol. 33, no. 3, pp. 803–807, 1995.

[28] A. M. Neville, *Properties of Concrete*, Longman, Harlow, UK, 1995.

[29] J. PH. Poley, J. J. Nooteboom, and P. J. de Waal, "Use of V.H.F. dielectric measurements for borehole formation analysis," *Log Analyst*, vol. 19, no. 3, pp. 8–30, 1978.

[30] A. Von Hippel, Ed., *Dielectric Materials and Applications*, Technology Press of MIT, Cambridge, Mass, USA, 1995.

[31] J. Q. Shang and J. A. Umana, "Dielectric constant and relaxation time of asphalt pavement materials," *Journal of Infrastructure Systems*, vol. 5, no. 4, pp. 135–142, 1999.

[32] K. S. Cole and R. H. Cole, "Dispersion and absorption in dielectrics I. Alternating current characteristics," *The Journal of Chemical Physics*, vol. 9, no. 4, pp. 341–351, 1941.

[33] G. P. de Loor, "Dielectric properties of wet materials," *IEEE Transactions on Geoscience and Remote Sensing*, vol. 21, no. 3, pp. 364–369, 1982.

[34] J. B. Hasted, *Aqueous Dielectrics*, Chapman and Hall, London, UK, 1973.

[35] N. J. Cassidy, "Electrical and magnetic properties of rocks, soils and fluids," in *Ground Penetrating Radar: Theory and Applications*, H. M. Jol, Ed., chapter 2, Elsevier, Amsterdam, The Netherlands, 2009.

[36] J. R. Wang and T. J. Schmugge, "An empirical model for the complex dielectric permittivity of soils as a function of water content," *IEEE Transactions on Geoscience and Remote Sensing*, vol. 18, no. 4, pp. 288–295, 1980.

[37] J. A. Huisman, S. S. Hubbard, J. D. Redman, and A. P. Annan, "Measuring soil water content with ground penetrating radar: a review," *Vadose Zone Journal*, vol. 2, pp. 476–491, 2003.

[38] L. J. West, K. Handley, Y. Huang, and M. Pokar, "Radar frequency dielectric dispersion in sandstone: implications for determination of moisture and clay content," *Water Resources Research*, vol. 39, no. 2, pp. 1026–1037, 2003.

[39] P. Hoeskstra and W. T. Doyle, "Dielectric relaxation of surface absorbed water," *Journal of Colloidal and Interface Science*, vol. 79, no. 11, pp. 1699–1708, 1971.

[40] M. C. Dobson, F. T. Ulaby, M. T. Hallikainen, and M. A. El-Rayes, "Microwave dielectric behavior of wet soil—part II: dielectric mixing models," *IEEE Transactions on Geoscience and Remote Sensing*, vol. 23, no. 1, pp. 35–46, 1985.

[41] M. T. Hallikainen, F. T. Ulaby, M. C. Dobson, M. A. El-Rayes, and L. Wu, "Microwave dielectric behavior of wet soil—part I: emprical models and experimental observations," *IEEE Transactions on Geoscience and Remote Sensing*, vol. 23, no. 1, pp. 25–34, 1985.

[42] M. A. Fam and M. B. Dusseault, "High-frequency complex permittivity of shales (0.02–1.30 GHz)," *Canadian Geotechnical Journal*, vol. 35, no. 3, pp. 524–531, 1998.

[43] S. P. Friedman, "A saturation degree-dependent composite spheres model for describing the effective dielectric constant of unsaturated porous media," *Water Resources Research*, vol. 34, no. 11, pp. 2949–2961, 1998.

[44] S. Qian and D. Chen, *Joint Time-Frequency Analysis: Methods and Applications*, Prentice Hall, Upper Saddle River, NJ, USA, 1996.

[45] A. P. Annan, "Ground penetrating radar," in *Near-Surface Geophysics*, D. K. Butler, Ed., chapter 11, Society of Exploration Geophysics, 2005.

[46] A. Shaari, S. G. Millard, and J. H. Bungey, "Modelling the propagation of a radar signal through concrete as a low-pass filter," *NDT and E International*, vol. 37, no. 3, pp. 237–242, 2004.